BNL-227549-2025-TECH

CA/AP/714

Maximizing RHIC Deliverable Luminosity with Dynamic Telescopic Beta* Squeeze

G. Robert-Demolaize

January 2025

Collider Accelerator Department

Brookhaven National Laboratory

U.S. Department of Energy

USDOE Office of Science (SC), Nuclear Physics (NP)

DISCLAIMER

Maximizing RHIC Deliverable Luminosity with Dynamic Telescopic Beta* Squeeze

Guillaume Robert-Demolaize,* Angelika Drees, Xiaofeng Gu, Al Marusic, and Steve Tepikian
Brookhaven National Laboratory (BNL), Upton, NY, USA

Mei Bai
GSI, Darmstadt, Germany

Simon White
ESRF, Grenoble, France
(Dated: March 8, 2018)

To benefit fully from the exceptional performance of the Relativistic Heavy Ions Collider (RHIC) Stochastic Cooling system during heavy ions physics store, the betatron amplitude β^* at a given collision point (IP) can be squeezed from its design value by using the available space in the quadrupole triplets from smaller beam emittances. This should allow reaching new heights in deliverable luminosity for both STAR and PHENIX experiments. Prior to 2014, RHIC lattice designs only squeezed the interaction regions (IR's) down to $\beta^* = 0.70$ m. To get past this limitation, one can use a telescopic scheme where the non-experimental insertions surrounding STAR and PHENIX are used to generate and close a β-beat wave contributing to the final squeeze in the two IP's of interest. The following presents the various steps of the implementation in RHIC of this telescopic scheme and the corresponding changes in collision rates and specific luminosity. A full feasibility study with a review of hardware and beam dynamics limitations is also included.

I. INTRODUCTION

The main performance parameters of a collider are the energy of the circulating beams E and the luminosity $\mathcal{L}$. For a given physics process of cross section σ_p, the event rate R is given by:

$$\frac{dR}{dt} = \mathcal{L} \cdot \sigma_p \ . \tag{1}$$

In the particular case of equal Gaussian bunched beams colliding head-on [1]:

$$\mathcal{L} = \frac{N_1 N_2 f N_b}{4\pi \sigma_x^* \sigma_y^*} \ , \tag{2}$$

where $\sigma^*_{x,y}$ is the transverse beam size in each plane at the interaction point (IP), $N_{1,2}$ is the number of particles per bunch for each beam, f the revolution frequency and N_b the number of colliding bunches. The cross section σ_p for rare events is small, which means a larger luminosity $\mathcal{L}$ is required to detect such events. This can be achieved with smaller beam sizes:

$$\sigma_x^* = \sigma_y^* = \sqrt{\beta_x^* \cdot \epsilon_x} = \sqrt{\beta_y^* \cdot \epsilon_y} = \sqrt{\beta^* \cdot \epsilon} \quad , \tag{3}$$

where $\beta^*_{x,y}$ is the betatron function in each plane at the IP and $\epsilon_{x,y}$ the emittance in each plane. For unequal beams, Equation 2 becomes [1]:

$$\mathcal{L} = \frac{N_1 N_2 f N_b}{2\pi \sqrt{(\sigma_{x1}^*)^2 + (\sigma_{x2}^*)^2} \sqrt{(\sigma_{y1}^*)^2 + (\sigma_{y2}^*)^2}} \ . \tag{4}$$

Equation 4 shows that reaching higher luminosity can be achieved by reducing either β^* or ϵ for each beam if all other machine parameters are kept the same.

RHIC is designed to operate with polarized protons p↑ as well as heavy ions A, generating either symmetric (p↑-p↑) or asymmetric (p↑-A, A_1-A_2) collisions. Since 2010, for operations with heavy ions, a Stochastic Cooling (SC) [2–4] system allows reducing the transverse beam emittances $\epsilon_{x,y}$ over the duration of a physics store, for either one or both beamlines. If the betatron functions at the quadrupole triplets of each experimental insertion can in turn be increased at the same rate so as to reduce the β^* at each IP, luminosity leveling would then be possible. Such a dynamic β^* squeeze mechanism would maximize the delivered integrated luminosity for each store.

Table I reviews the β^* and $\epsilon_{\rm rms}$ values achieved during the most recent RHIC high energy heavy ions runs up to 2016 [5]; the peak luminosity delivered to the STAR (IR6) and PHENIX (IR8) experiments is also reported. Since 2007, benefiting from larger beam intensities delivered by the injector chain as well as smaller optics at the STAR and PHENIX IP's, the peak luminosity in RHIC went up by about a factor 5; the peak luminosity achieved in 2012 is larger than 2014 only because of the stored intensity of the Cu beam, three times as much as the Au beam. Part of this significant improvement should also be attributed to the increased performance of the RHIC feedback systems used for the ramp in energy in the main ring, during which transmission efficiencies are consistently over 90%.

Since its initial commissioning in 2007 [6], the RHIC SC system has improved both in performance and reliability. Figure 1 shows the evolution of the transverse emittances for the Blue and Yellow beams during one of the 100 GeV Au^{79+} stores in 2011 and 2014. The

* grd@bnl.gov

TABLE I. Overview of performance parameters for the most recent 100 GeV RHIC runs with Au^{79+} [5].

Run	2007	2010	2011	2012	2014	2016
Species	Au-Au	Au-Au	Au-Au	Cu-Au	Au-Au	Au-Au
Total Intensity [10^9]	113.3	122.1	144.3	444.0 (Cu) 144.3 (Au)	177.6	222.0
β^* (IR6/8) [m]	0.83/0.77	0.75/0.75	0.75/0.75	0.70/0.70	0.70/0.70 → 0.50/0.50	0.70/0.70
$\epsilon_{\rm rms}$ [μm]	2.8 → 5.8	2.8 → 3.3	2.5 → 1.7	4.1 → 1.2	2.5 → 0.65	2.0 → 0.7
$L_{\rm peak}$ [10^{26} cm^{-2} s^{-1}]	30.0	45.3	52.6	120.0	84.0	155.0

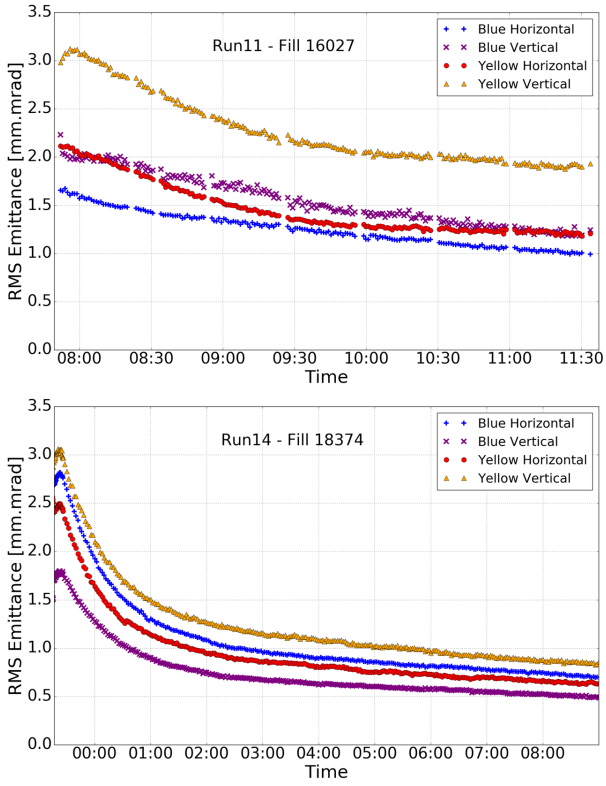

FIG. 1. Horizontal and vertical transverse emittances of the Blue and Yellow beams for a typical RHIC 100 GeV Au-Au store with stochastic cooling on during the 2011 (top) and 2014 (bottom) operations. The improvements brought to the system between those two runs can clearly be seen when comparing the slopes of each curve.

effect of the SC system is clearly apparent, and shows significant improvement in 2014 and 2016 since its initial operation in 2007. Based on the data shown in Figure 1, it is clear that squeezing β^* can only be done in the later part of a store: the transverse emittances first have to be significantly reduced to not risk losing the beam in the machine aperture due to increasing β functions in the triplets while currents are ramping up in the quadrupoles selected for the squeezing algorithm.

The following reviews in details the newly designed dynamic β^* squeeze scheme for RHIC. Section II discusses the concepts and implications for the lattice. Section III presents the results of the first tests during dedicated beam experiment time as well as end-of-store activities. Section IV describes the practical considerations for an implementation as part of regular RHIC operations, and provides the analysis of the luminosity data acquired when the dynamic β^* squeeze was used.

II. THEORETICAL CONCEPT

A. Initial design

Studies for a dynamic β^* squeeze at RHIC were performed toward the end of the 2011 operations [7]. Initially, only the STAR insertion (IR6) was considered, since both experimental regions are identical in terms of machine design i.e. magnet types and power supply (PS) wiring scheme. Figure 2 presents the wiring scheme of the PS's of all quadrupole magnets of the STAR interaction region [8]. A similar scheme can be found in other interaction regions: IR8 (PHENIX experiment), IR2 and IR12. The remaining insertions, IR4 (dedicated to the RHIC RF system) and IR10 (where the newly installed and commissioned RHIC e-lens devices [9, 10] are located), feature a left/right split of the scheme around the IP.

The principle of this wiring scheme relies on nested PS's: aside from the trim quadrupole magnets TQ4, TQ5 and TQ6 which are equipped with individual PS's, the total current in each IR quadrupole is the sum of the current in the main bus line ($I_{\rm QF}$ for Q1-7, $I_{\rm QD}$ for Q8-9) and all shunt supplies around it, as shown in Figure 2. For example, the current in each Q1 (the quadrupole closest to the IP) is given by:

$$I_{\rm Q1} = I_{\rm QF} + \sum_{n=1}^{7} I_{\rm shunt}\left(Q_n\right) \ . \qquad (5)$$

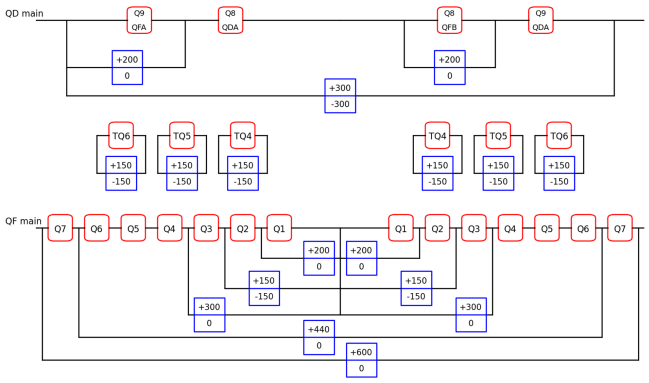

FIG. 2. Wiring scheme of the quadrupole magnets power supplies in the STAR (IR6) insertion of RHIC. Upper and lower current limits are included. From [8].

One should also note from the wiring scheme that the total circulating current - and therefore the integrated gradient KL - in each of the three quadrupole magnets Q4-6 is the same since they share the same shunt PS.

The main idea behind the initial squeeze test RHIC in 2011 was to define a section of the machine over which the phase advance would remain constant while the quadrupole gradients in IR6 (STAR experiment, for which the test was conducted) are adjusted to lower β^*. From Figure 2, it is clear that such a section should be located in between the Q9 magnets that define the beginning and end of the IR6 straight section. The advantage is that the tunes Q_x and Q_y are left unchanged since the free parameters are the currents in the shunt PS's and the main PS bus lines are not included. Overall the 2011 experimental results [7] clearly demonstrated a proof of principle, as the measured luminosity increase (13.72%) was in good agreement with the predicted one (17.14%).

B. β^* squeeze using telescopic optics

The Achromatic Telescopic Squeeze (ATS) scheme has been developed at CERN as part of the development studies for the Large Hadron Collider (LHC) upgrade [11, 12]. The concept of ATS is to use the IR's around the targeted experimental insertion to launch and close a β-beat wave to allow reducing the β^* further with little to no change to the chromatic functions. ATS requires a 90° FODO lattice and phase advance of $k\pi/2$ ($k = 1 \ldots N$) between the targeted IP and both focusing and defocusing sextupole families for the ideal chromaticity correction scheme. However, the RHIC lattice was designed with the STAR and PHENIX IR's downstream of one another. For the ATS scheme implementation, this adds another phase advance constraint for the β-beat wave to be effective at both IP's at the same time:

$$\Delta\phi\,(\text{STAR} \leftrightarrow \text{PHENIX})_{\text{ATS}} = k\pi,\ k = 1 \ldots N\ . \quad (6)$$

When preparations for the 2014 operations started, the decision was made to use the RHIC lattice for Uranium-Uranium collisions from 2012 as a baseline. To date, this lattice had offered the best performance in terms of dynamic aperture and integrated luminosity for RHIC high energy A-A runs [13]; it unfortunately does not meet the ATS requirements described so far. However, the general concept of the β-beat wave can still be applied if one uses a global rematching algorithm over a section of the machine that includes the STAR and PHENIX IR's as well as the IR's immediately downstream and upstream, i.e. from IR4 to IR10 (see Figure 3). For the rest of this article, this segment of the lattice will be referred to as the 'ATS region'.

Another feature of the RHIC lattice for Au-Au 100 GeV collisions is the operation of the SC system. Per its design [2, 3], all pickup/kicker pairs for each transverse plane have to be separated by a $\pi/2$ phase advance. As shown in Figure 3 [14], some of this equipment is located in IR4 i.e. in one of the insertion regions required for ATS. This makes for additional constraints when rematching the lattice for ATS implementation, since squeezed optics can only be implemented with lower transverse emittances from a fully performing SC system.

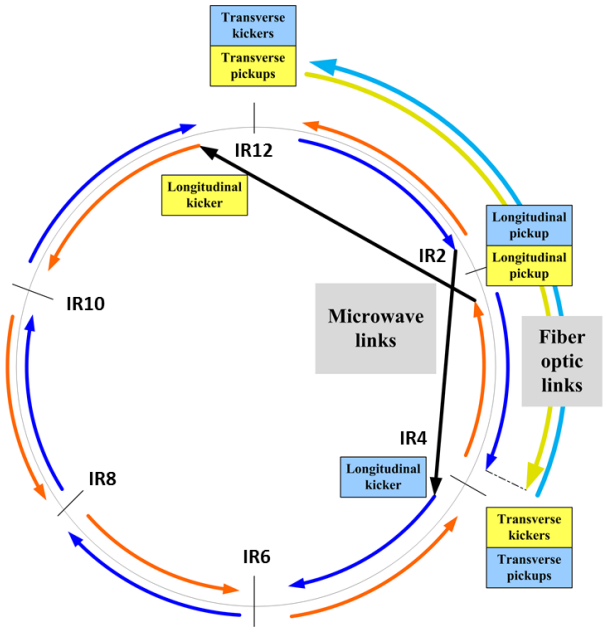

FIG. 3. Schematic view of the locations of the RHIC interaction regions (IR's) and the Stochastic Cooling equipment. From [14].

Taking into account all theoretical concepts and machine specific requirements, Figures 4 and 5 show the baseline and ATS linear optics for the Blue and Yellow lattices designed for the 2014 RHIC operations as calculated by MAD-X[15], with β^*(IR6,IR8) = 0.5 m for the squeezed optics. Additional studies showed that a linear optics design with β^*(IR6,IR8) = 0.35 m is achievable

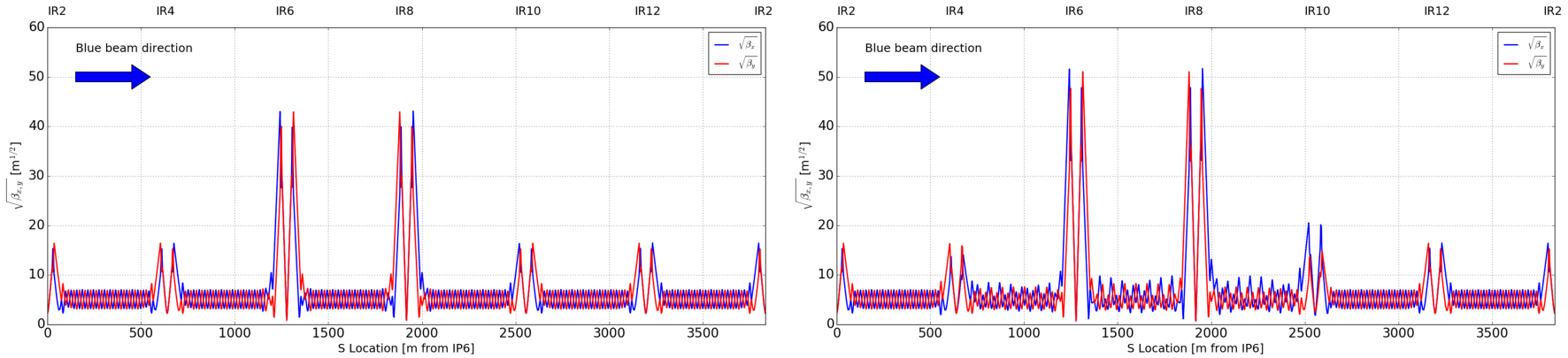

FIG. 4. Comparison of the linear $\beta_{x,y}$ functions (top) and horizontal dispersion D_x (bottom) of the Blue lattice between the baseline optics with β^* (IR6,IR8)=0.7m (left) and ATS optics with β^* (IR6,IR8)=0.5m (right) as designed for the 2014 RHIC Au-Au 100 GeV collisions. The β-beat wave generated for the ATS optics can be seen starting from IR4 and collapsing at IR10.

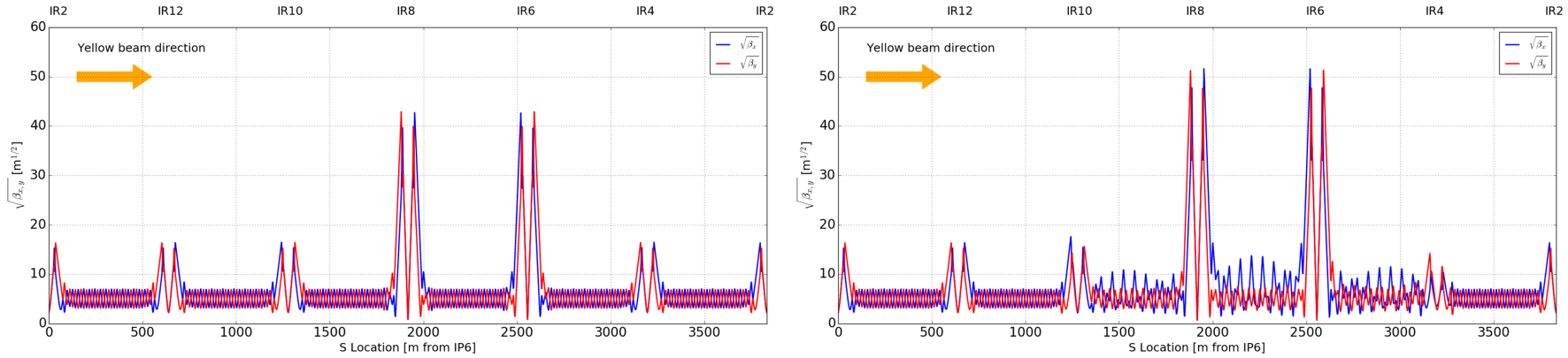

FIG. 5. Comparison of the linear $\beta_{x,y}$ functions (top) and horizontal dispersion D_x (bottom) of the Yellow lattice between the baseline optics with β^* (IR6,IR8)=0.7m (left) and ATS optics with β^* (IR6,IR8)=0.5m (right) as designed for the 2014 RHIC Au-Au 100 GeV collisions. The β-beat wave generated for the ATS optics can be seen starting from IR4 and collapsing at IR10.

with the existing RHIC quadrupole PS Scheme; however the corresponding limitations on dynamic aperture from non-linear beam dynamics would affect the deliverable integrated luminosity to the experiment in such a way that it would negate the gain in peak luminosity.

Table II compares the linear optics functions of the ATS and baseline lattices. In both cases, the largest β functions can be found at the triplet quadrupoles in the STAR and PHENIX insertions: in the ATS case, $\beta_{x,y}$ is about 45% larger than for baseline optics and operations. With Equation 3, the beam is therefore 20% larger in the triplets; using the data from Table I, and assuming that the ATS optics would be applied once the transverse emittances are stabilized to their lowest values $\epsilon_{\rm SC}$, the transverse beam size would become:

$$\begin{aligned}\sigma^{\rm peak}_{\rm x,y}({\rm baseline}) &= \sqrt{\beta^{\rm peak}_{\rm x,y}\cdot\epsilon_{\rm SC}} \approx 3.353 \text{ mm},\\ \sigma^{\rm peak}_{\rm x,y}({\rm ATS}) &= \sqrt{\beta^{\rm peak}_{\rm x,y}\cdot\epsilon_{\rm SC}} \approx 4.021 \text{ mm}.\end{aligned} \tag{7}$$

All triplet quadrupoles have a circular transverse mechanical aperture, with a radius $r_{Q1-3} = 56.365$ mm, which gives for the available aperture $A_{x,y}$:

$$\begin{aligned}A_{\rm x,y}({\rm baseline}) &= 16.810\cdot\sigma^{\rm peak}_{\rm x,y}({\rm baseline}),\\ A_{\rm x,y}({\rm ATS}) &= 14.018\cdot\sigma^{\rm peak}_{\rm x,y}({\rm ATS}).\end{aligned} \tag{8}$$

With a typical beam size of 5-6 $\sigma_{x,y}$ during RHIC operations, those numbers show that there is enough clearance to accommodate for the larger β functions from the ATS optics. It can also be noted from Figures 4 and 5 that the dispersion function D_x is nearly canceled in the STAR and PHENIX insertions for the ATS optics, which provides additional transverse off-momentum aperture.

C. Chromatic correction

As with any attempt to squeeze β^* further than the initial design, one has to be mindful of the chromatic aberrations that come as a consequence of higher $\beta_{x,y}$ functions in the triplet quadrupoles of the experimental IR's, as well as the off-momentum β-beating in all other sections of the lattice. Detailed studies [11] have already showed that if the initial (pre-squeeze) lattice is rematched with the appropriate phase advance requirements between quadrupole and sextupole families, it is possible to achieve a passive compensation of chromatic effects when applying the ATS settings.

As introduced in the section II B, although the RHIC lattices do not feature those phase advance requirements, the number of available sextupole families should allow for both linear and non-linear chromaticity corrections. In total, for each RHIC beamline there are 24 families that can be controlled individually, with 2 focusing (SXF) and 2 defocusing (SXD) families per arc.

Figure 6 shows a schematic view of how these sextupoles are split around the ring:

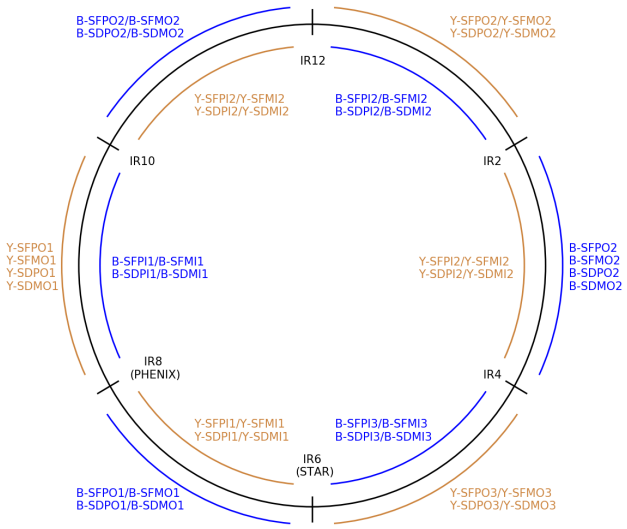

FIG. 6. Schematic representation of the locations of all RHIC sextupole families: up to 4 families per arc, i.e. 24 families per ring, can be used for chromaticity control

- B/Y refers to the Blue or Yellow lattice;
- F/D indicates if the considered family is focusing or defocusing;
- P/M allows to get either one or two families per arc, if SX[F/D]P $\neq$ SX[F/D]M;
- I/O for the location, Inner or Outer arc.

The linear chromaticities $Q'_{x,y}$ in a circular accelerator are given by [16]:

$$Q'_{x,y} = \frac{1}{4\pi}\oint \beta_{x,y}(s)\left[\mp K_1(s) \pm K_2(s)D_x(s)\right]ds\ , \tag{9}$$

where $K_1(s)$ and $K_2(s)$ are the gradients (or strengths) of the RHIC quadrupole and sextupole magnets respectively, and $D_x(s)$ is the dispersion function. The knob to control $Q'_{x,y}$ uses gradient changes $\Delta K2_{\rm SXF}$ and $\Delta K2_{\rm SXD}$ common to each SXF and SXD families, with a response matrix R_2 such that:

$$\begin{aligned}\begin{pmatrix}\Delta Q'_x\\ \Delta Q'_y\end{pmatrix} &= R_2\cdot\begin{pmatrix}\Delta K2_{\rm SXF}\\ \Delta K2_{\rm SXD}\end{pmatrix}\\ &= \begin{pmatrix}r_{1,1} & r_{1,2}\\ r_{2,1} & r_{2,2}\end{pmatrix}\cdot\begin{pmatrix}\Delta K2_{\rm SXF}\\ \Delta K2_{\rm SXD}\end{pmatrix},\end{aligned} \tag{10}$$

where $\Delta Q'_x$ and $\Delta Q'_y$ are the requested chromaticity changes. By splitting $K2_{\rm SXF}$ and $K2_{\rm SXD}$ into their respective individual families as shown in Figure 6, one gets a new response matrix R^B_{24} defined for the Blue beam as:

TABLE II. Comparison between the linear optics functions in RHIC between the ATS lattice and the design (baseline) lattice. Data is given for both Blue and Yellow lattices.

	Blue lattice		**Yellow lattice**	
Parameter	**ATS optics**	**Baseline optics**	**ATS optics**	**Baseline optics**
β^*(IR6,IR8)	0.5 m	0.7 m	0.5 m	0.7 m
$\beta_{x,y}^{\mathrm{MAX}}$	2670.90 m (H) 2605.17 m (H)	1857.47 m (H) 1843.13 m (V)	2662.66 m (H) 2633.39 m (H)	1825.84 m (V) 1841.66 m (V)
$(\Delta\beta/\beta)_{\mathrm{RMS}}$	45.33% (H) 23.26% (V)		91.86% (H) 33.18% (V)	
$(\Delta\beta/\beta)_{\mathrm{peak}}$ [absolute value]	115.78% (H) 49.88% (V)		290.08% (H) 145.03% (V)	
$(\Delta\beta/\beta)_{\mathrm{RMS}}^{\mathrm{arc}}$	47.04% (H) 19.31% (V)		124.95% (H) 21.65% (V)	
$(\Delta\beta/\beta)_{\mathrm{peak}}^{\mathrm{arc}}$ [absolute value]	95.41% (H) 43.58% (V)		290.08% (H) 49.49% (V)	

$$\begin{pmatrix}\Delta Q'_x\\ \Delta Q'_y\end{pmatrix}_B = R_{24}^B \cdot \begin{pmatrix}\Delta K2_{\text{B-SFPO1}}\\ \vdots \\ \Delta K2_{\text{B-SDMI3}}\end{pmatrix} = \begin{pmatrix} r_{1,1}^B & \dots & r_{1,24}^B \\ r_{2,1}^B & \dots & r_{2,24}^B \end{pmatrix} \cdot \begin{pmatrix}\Delta K2_{\text{B-SFPO1}}\\ \vdots \\ \Delta K2_{\text{B-SDMI3}}\end{pmatrix} . \quad (11)$$

Shifting from Equation 10 to Equation 11 creates additional degrees of freedom so that the calculated ΔK_2 of each sextupole family can take into account the β-beat wave generated by the ATS scheme (as shown in Figure 4 and Figure 5). For the remainder of Section II C and for practical purposes, simulations and experimental results will be given for the Blue lattice of RHIC only; similar results could be derived for the Yellow lattice.

The amplitude of the non-linear chromatic terms needs to be kept under control in order to maximize the off-momentum dynamic aperture. By taking the partial derivative in δ of Equation 9, one gets:

$$Q_{x,y}^{(2)} = \frac{\partial Q'_{x,y}}{\partial \delta} = -\frac{1}{2}Q'_{x,y} + \frac{1}{8\pi}\oint \left[\mp K_1(s) \pm K_2(s)D_x(s)\right]\frac{\partial \beta_{x,y}(s)}{\partial \delta}ds + \frac{1}{8\pi}\oint \pm K_2(s)\beta_{x,y}(s)\frac{\partial D_x(s)}{\partial \delta}ds \quad (12)$$

Even though the analytical formula from Equation 12 could be used in an optimizing algorithm, minimization methods are readily available in MAD-X. One such method is to analyze the changes $\Delta Q_{x,y}$ in betatron tunes of particles with a given momentum deviation $|\delta| = |dp/p_0|$. Figure 7 shows the results of calculations performed for $|\delta| \leqslant 2.5\text{x}10^{-3}$ using the 2016 Au-Au lattice. A convenient formulation of the tune shifts due to momentum offsets is to consider their dependence on chromatic effects as a Taylor series and write it as:

$$\Delta Q_{x,y}(\delta) = Q'_{x,y}\delta + Q_{x,y}^{(2)}\delta^2 + Q_{x,y}^{(3)}\delta^3 + ... \quad (13)$$

where $Q_{x,y}^{(i)}$ is the i^{th} order chromaticity. In the context of RHIC physics runs, non-linear chromaticity correction aims at minimizing $Q_{x,y}^{(2)}$ and $Q_{x,y}^{(3)}$ while keeping $Q'_{x,y} = 2.0$. In Figure 7, the deviation from these ideal lattice conditions can be measured by the size of the colored areas, which are correlated to $Q_{x,y}^{(2)}$ and $Q_{x,y}^{(3)}$ as given

in Equation 13. Consequently, one can create a correction algorithm in MAD-X using all RHIC sextupole families listed previously and apply polynomial fits so that $\Delta Q_{x,y}(\delta) = 2\delta$. The results of such fits can be seen in Figure 8, which features $Q^{(2)}_{x,y} < 100.0$, i.e. close to ideal lattice settings for dynamic aperture purposes.

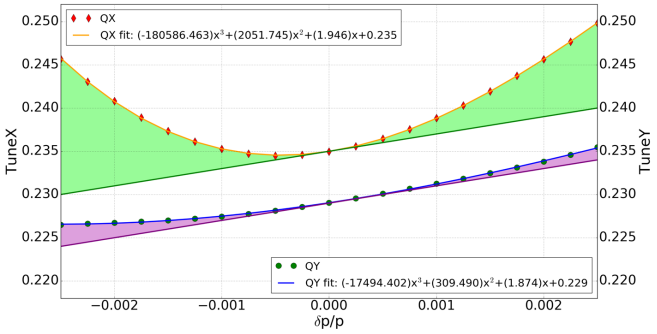

FIG. 7. Horizontal (diamond markers) and vertical (round markers) betatron tunes of the 2016 Au-Au 100 GeV Blue lattice as function of the momentum offset $\delta p/p$. The colored areas highlight the deviation to ideal lattice conditions where the linear chromaticity is 2.0 and the 2$^{\text{nd}}$ and 3$^{\text{rd}}$ order chromaticities are canceled.

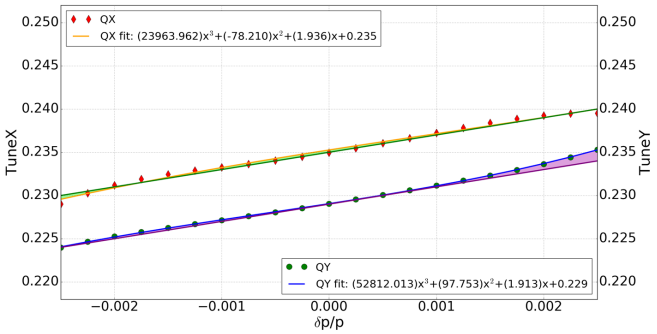

FIG. 8. Horizontal (diamond markers) and vertical (round markers) betatron tunes of the 2016 Au-Au 100 GeV Blue lattice as function of the momentum offset $\delta p/p$ once the non-linear chromaticity correction algorithm developed in MAD-X is applied to the data from Figure 7.

Table III presents a summary of all chromaticity-related calculations discussed in this section, as well as the results of the experimental implementation of the non-linear chromaticity correction scheme. The **Design** part of Table III relates to the MAD-X model description of RHIC as designed for 2016: the initial settings of the sextupoles are optimized for linear chromaticities $Q'_{x,y}$ close to 2.0, however the non-linear terms are large especially in the horizontal plane with $Q^{(2)}_{x,y} > 2000.0$. As mentioned previously and seen in Figure 8, a first round of correction with the new MAD-X algorithm (**Step 1**) leads to linear chromaticities essentially unchanged (less than 2.0% difference) while lowering the non-linear terms to less than 100.0 units in absolute values.

TABLE III. Amplitude of the linear and non-linear chromaticity terms of the 2016 RHIC lattice for the Design lattice (derived from MAD-X) and from measurements during regular machine operations.

	Q'_x	Q'_y	$Q^{(2)}_x$	$Q^{(2)}_y$
Design	1.95	1.87	2051.74	309.49
Correction - Step 1	1.94	1.91	-78.21	97.75
Correction - Step 2	1.91	1.92	-817.21	80.90
Measured	3.38	2.36	3869.00	-715.00
Correction - Step 1	3.90	1.8	2207.00	-742.00
Correction - Step 2	0.29	0.20	844.00	-898.00

Actual measurements in RHIC of the chromaticities during 2016 operations are reported in the **Measured** part of Table III: the largest deviations from the theoretical model are in the horizontal plane, with $Q^{(2)}_x$ spiking to close to 4000.0 units. When implementing the design changes of strength to the sextupole families for **Step 1** of the correction, it can be seen that $Q^{(2)}_x$ is not brought down close to zero, but the amplitude of change ($\Delta = -1662.0$ units) is in the same range than what is calculated for **Design** ($\Delta = -2129.95$ units). From this first attempt, it was determined that lowering the non-linear terms in RHIC would require forcing these same terms even lower in MAD-X simulations: the second attempt at correction, **Step 2**, aims to do just that all while keeping the polarities of the sextupole families as is[1]. When applying the magnet settings derived for **Step 2**, the non-linear terms $Q^{(2)}_{x,y}$ did change by an amount equivalent to what is predicted: $\Delta Q^{(2)}_x = -3025.00$ units (compared to -2868.95 requested from **Design**) and $\Delta Q^{(2)}_y = -183.00$ units (-228.59). This correction puts the Blue lattice in an optimal non-linear chromaticity space, with $|Q^{(2)}_{x,y}| < 1000.0$, but it also alters the linear terms enough to put the lattice closer to coherence instabilities ($Q'_{x,y} \approx 0.0$).

While the benefits of this method to the dynamic aperture are clear, the correction scheme still needs to be

[1] additional simulations showed that it is theoretically possible to reach very low measured $Q^{(2)}_{x,y}$ values if the polarity of one of the sextupole families was flipped, from focusing to defocusing; for practical reasons, this was not attempted in 2016 to instead maximize the uptime of physics stores.

worked through some more iterations to ensure the linear chromaticity changes remain tolerable before a full integration to regular machine operations.

D. Hourglass Factor

The definition of luminosity given in Equation 2 only applies at the IP and does not fully take into account how the transverse beam sizes $\sigma_{x,y}$ change along the bunch length. Figure 9 shows the shape of $\beta_{x,y}(s)$ as a function of β^*; negative values, though unrealistic, are displayed as illustration of how rapidly the beam size changes with s when β^* is squeezed. A correction coefficient known as the Hourglass factor H can be applied, making the luminosity read[1]:

$$\begin{aligned}\mathcal{L} &= \left(\frac{N_1 N_2 f N_b}{4\pi\sigma_x^*\sigma_y^*}\right)\cdot H \\ &= \left(\frac{N_1 N_2 f N_b}{4\pi\sigma_x^*\sigma_y^*}\right)\frac{\cos\frac{\phi}{2}}{\sqrt{\pi}\sigma_s}\int_{-\infty}^{+\infty}\frac{e^{-s^2 A}}{1+(\frac{s}{\beta^*})^2}ds\end{aligned} \tag{14}$$

with ϕ the crossing angle between the two beams in the horizontal plane, and:

$$A = \frac{\sin^2\frac{\phi}{2}}{(\sigma_x^*)^2\left[1+(\frac{s}{\beta^*})^2\right]} + \frac{\cos^2\frac{\phi}{2}}{\sigma_s^2} \tag{15}$$

where σ_s is the longitudinal beam size and $\sigma_s >> \sigma_x^*$.

TABLE IV. Hourglass Factor H and Luminosity ratio $\mathcal{L}(\beta^*)/\mathcal{L}(0.7)$ as per Equations 14 as a function of β^* for Au-Au collisions at $\sqrt{s_{NN}}$ =200 GeV, assuming $\phi = 0.0$, $\sigma_s = 6.5$ ns, and $\epsilon_x = 0.65$ μm.

β^*[m]	H	$\mathcal{L}(\beta^*)/\mathcal{L}(0.7)$
0.30	0.231	1.218
0.40	0.293	1.157
0.50	0.348	1.100
0.60	0.398	1.048
0.70	0.443	1.000
0.80	0.484	0.955
0.90	0.520	0.914
1.00	0.554	0.875
1.10	0.584	0.840

H can easily be calculated via numerical scripts for different β^* values. For 2014, the design value for β^* in the STAR and PHENIX insertions is set to 0.70 m, similar to previous high energy Au-Au physics runs; this setup can be used as a reference value when looking at changes in $\mathcal{L}$ with the Hourglass effect. Figure 9 and Table IV show the ratio $\mathcal{L}(\beta^*)/\mathcal{L}(0.7)$ for 100 GeV Au-Au runs, assuming head-on collisions i.e. $\phi = 0.0$. Using measurement data from 2014 around the time the dynamic β^* squeeze would be applied, the *rms* bunch length is σ_s = 6.5 ns; the transverse *rms* emittances can be taken $\epsilon_{x,y}$ = 0.65 μm using Figure 1. As described in section II B, the plan is to squeeze β^* in IR6 and IR8 from 0.70 m to 0.50 m, for which a 10% increase in delivered luminosity is predicted.

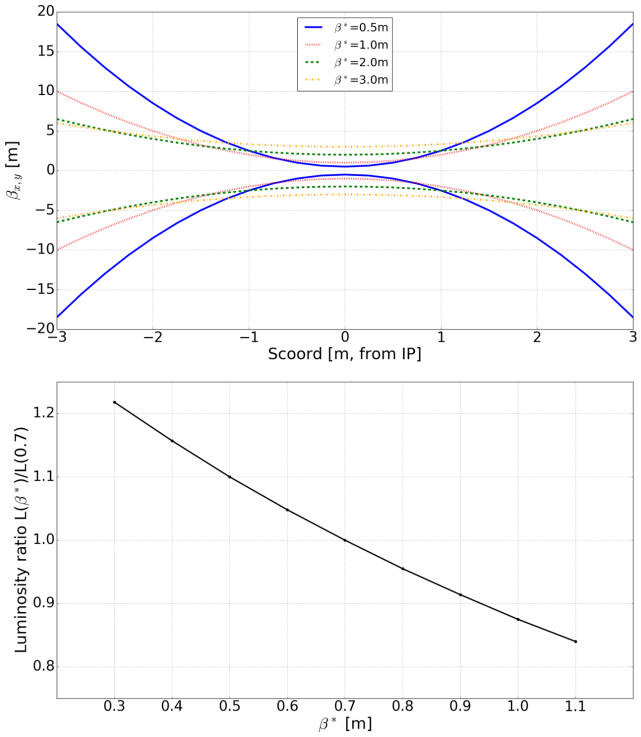

FIG. 9. Top: Changes in $\beta_{x,y}$ around a given interaction point (IP) for different values of the minimum β^* required at that IP: the overall shape of the betatron functions is what gave its name to the *Hourglass effect*. - Bottom: Luminosity ratio $\mathcal{L}(\beta^*)/\mathcal{L}(0.7)$ calculated from Equation 14 as a function of β^*: a squeeze from 0.70 m to 0.50 would provide a 10% gain in delivered luminosity.

III. EXPERIMENTAL COMMISSIONING

A. Measurement and correction of the RHIC linear optics

The quadrupole strengths required for the implementation of the ATS scheme described in Section II B are derived from the design RHIC linear optics at top energy; it is highly relevant to ensure that the pre-squeezed lattices are as close to their design as possible. Therefore the first step of the experimental commissioning of the RHIC ATS optics is to measure and (if need be) correct

the Blue and Yellow linear optics. For the remainder of Section III and for brevity, experimental results will be given for the Blue lattice of RHIC only.

Among all available linear optics measurement methods for circular accelerators [17], the one used at RHIC is the analysis of turn-by-turn closed orbit oscillations at beam position monitors (BPM's) locations. A Graphical User Interface tool, *loptics*, was developed to perform this analysis "live" during RHIC physics runs [18]. There are two ways to observe closed orbit oscillations around a given lattice: using an AC dipole to adiabatically drive coherent transverse oscillations at a frequency close to the betatron tunes $Q_{x,y}$; or using a single turn kicker magnet to generate a coherent beam excitation leading to free oscillations (similar to $Q_{x,y}$ measurements).

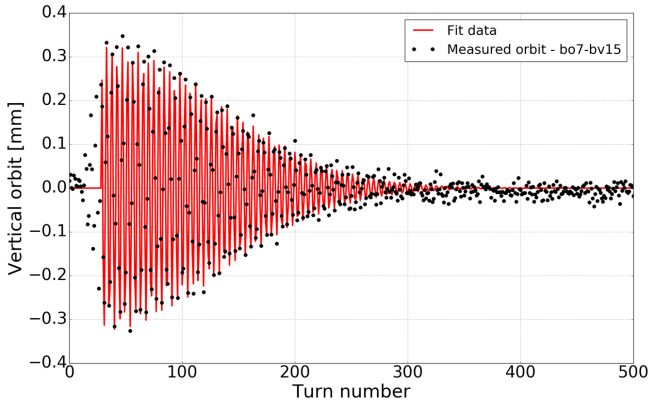

FIG. 10. Turn-by-turn vertical closed orbit oscillations (black markers) acquired at the vertical beam position monitor (BPM) labeled bo7-bv15 during Fill 18124 of 2014 RHIC operations. While closed orbit data is usually acquired over 1024 turns, only the first 500 turns of recorded oscillations are displayed here for relevance purposes. The corresponding non-linear fit (red solid line), from which the linear optic functions are derived, is included.

Figure 10 shows an example of measured free oscillations in the vertical plane of the Blue lattice, at the location of the bo7-bv15 BPM. One can clearly notice the exponential envelope of these oscillations: this damping effect comes from the linear vertical chromaticity Q'_y, and the number of turns during which the oscillations last gives an indication on the amplitude of Q'_y (but not its sign). For these free oscillations, the data acquired at each BPM can therefore be fitted as [19]:

$$z_i\left(N\right) = A_i^1 \exp\left[-2.0\left(\frac{\pi N}{A_i^2}\right)^2\right]\cos\left(\psi_z^i N + A_i^3\right) \quad (16)$$

where N is the turn number and $\psi_z^i = 2\pi\nu_z^i$ with ν_z^i the betatron tune at the i^{th} BPM as determined by FFT, z being either horizontal or vertical plane. The three parameters $A_i^{1,2,3}$ are determined using the Levenberg-Marquardt non-linear fitting algorithm [20], with A_i^1 and A_i^3 leading to the values of the betatron amplitude β_z and phase advance $\Delta\mu_z$ at the i^{th} BPM.

Performing non-linear fits to Equation 16 on the data gathered at each BPM location around the RHIC ring gives access to the linear optics of each lattice. Figure 11 shows the results of such an analysis for the Blue Au-Au 100 GeV lattice using a dataset of turn-by-turn data taken during Fill 18124 in 2014. By comparing the measured optics to the expected design value, one can derive the β-beat and the corresponding *rms* value in each plane.

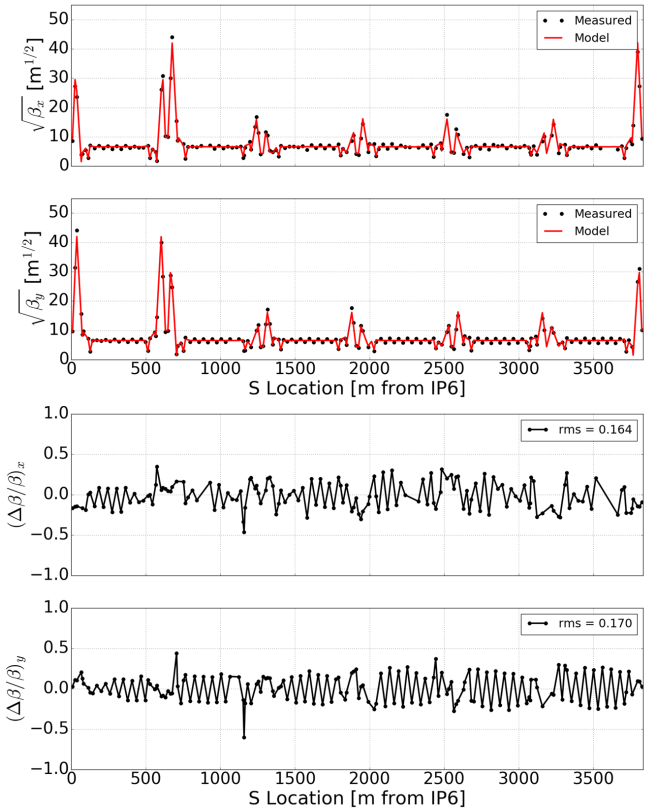

FIG. 11. Top: Measured horizontal (top) and vertical (bottom) $\sqrt{\beta}$ functions for the 2014 Blue Au-Au 100 GeV lattice (Fill #18124) compared to their design values from the RHIC Online Model. - Bottom: corresponding horizontal (top) and vertical (bottom) β-beat amplitude. The *rms* values of the deviations are given for each plane. All reported values are derived from the analysis of turn-by-turn closed orbit oscillations acquired at every BPM locations around the ring.

For the data displayed in Figure 11, the largest β-beat amplitudes are 33.16% in the horizontal plane and 29.81% in the vertical plane (in absolute value). These values are obtained after excluding the outlier BPM's reporting corrupted data[2]. In order to minimize this distortion, a response matrix $M_{p,q}$ is generated from the design settings of the considered lattice by selecting a group

[2] the datasets from the BPM's labeled bo7-b3.1 ($s \approx 573$ m), bi8-b3.1 ($s \approx 706$ m) and bi9-b7.1 ($s \approx 1158$ m) were reported as corrupted by the monitors' own hardware systems.

of q quadrupole magnets with individual power supplies (as described in section II A) to be used as a knob to correct the β-beat amplitudes $(\Delta\beta_z/\beta_z)_j$, $j = 1 \ldots p$ reported at p BPM's of that lattice. One can then apply Singular Value Decomposition (SVD) techniques to invert $M_{p,q}$ and get the required changes in quadrupole gradients (i.e. corrector strengths) ΔK_i, $i = 1 \ldots q$ [18]:

$$\begin{pmatrix} \Delta K_1 \\ \vdots \\ \Delta K_q \end{pmatrix} = -\left(M^{-1}_{p,q}\right) \cdot \begin{pmatrix} (\Delta\beta_z/\beta_z)_1 \\ \vdots \\ (\Delta\beta_z/\beta_z)_p \end{pmatrix}_{meas} . \quad (17)$$

Before implementing these correction strengths, *loptics* allows testing them as gradient errors to compare the resulting β-beat as predicted by the RHIC Online Model to what is measured in the machine. Figure 12 presents the result of this comparison for the data acquired during Fill 18124 along with the values of ΔK for the selected quadrupoles. The data clearly shows a strong agreement between the predicted and measured β-beat in both transverse planes; it should also be noted that the largest ΔK values are found at the location of the IR triplet quadrupoles Q_{1-3}. With this test completed, the correction strengths were implemented in RHIC for Fill 18127; the linear optics were measured once more and are shown in Figure 13.

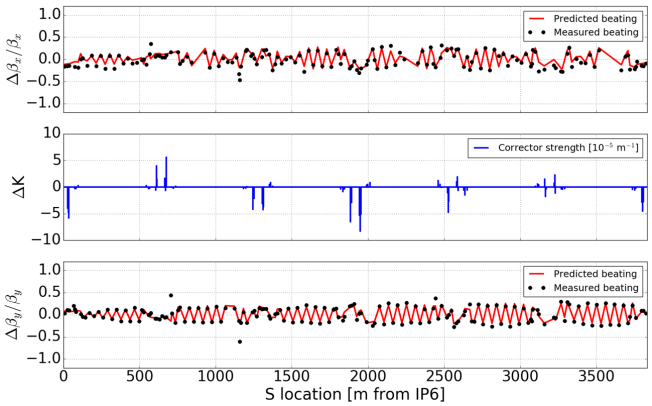

FIG. 12. Comparison between the predicted (solid line) and measured (black markers) β-beat in the horizontal (top) and vertical (bottom) plane of the Blue lattice, based on the calculated changes to quadrupole strengths (middle) for linear optics correction as derived from the analysis of the data acquired during Fill 18124 of 2014.

There is a significant change compared to the uncorrected linear optics from Figure 11: the peak β-beat amplitudes are now 27.59% in the horizontal plane and 22.44% in the vertical plane. More importantly, the most relevant mark of improvement is how much the *rms* value got lowered: from 0.164 to 0.097 (-40.8%) in the horizontal plane, and from 0.170 to 0.072 (-57.6%) in the vertical plane. These values clearly demonstrate that the RHIC linear optics were put much closer to the design settings.

In the context of the first experimental attempt at the ATS scheme, one parameter of particular interest is the amplitude of the $\beta_{x,y}$ functions at and around the STAR and PHENIX interaction points (IP's). Table V contains the results of calculations based on the linear optics measured during Fill 18124 (first measurement) and Fill 18127 (after correction). The values of $\beta_{x,y}$ at each IP, as well as their lowest values $\beta^*_{x,y}$ across each straight section, is determined by using the measurements at the Q_1 and D_x magnets around the considered IP and fitting according to the definition of the changes in $\beta_{x,y}$ in a straight section:

$$\beta_{x,y}(\Delta s) = \beta^*_{x,y} + \frac{\Delta s^2}{\beta^*_{x,y}} \quad (18)$$

where Δs is the distance between the interpolated $\beta_{x,y}$ and the IP. The improvement from linear optics correction can clearly be seen, not only in the values of $\beta_{x,y}$(IP) but also in $s^*_{x,y}$, which gives the relative position of $\beta^*_{x,y}$ to the IP. For the purpose of maximizing the luminosity $\mathcal{L}$(IP) delivered to each experiment, $s^*_{x,y}$ must be as close to zero as possible to avoid applying a geometric reduction factor G, derived from:

$$\begin{aligned} \sigma_{x,y}(\mathrm{IP}) &= \sqrt{\beta_{x,y}(\mathrm{IP}) \cdot \epsilon_{x,y}} \\ &= \sqrt{\beta^*_{x,y} \cdot \left(1 + \left(\frac{s^*_{x,y}}{\beta^*_{x,y}}\right)^2\right) \cdot \epsilon_{x,y}} \\ &= \sigma^*_{x,y} \cdot \sqrt{1 + \left(\frac{s^*_{x,y}}{\beta^*_{x,y}}\right)^2} \end{aligned} \quad (19)$$

which in turn leads to a modified Equation 2 that reads:

$$\mathcal{L}(\mathrm{IP}) = \mathcal{L} \cdot G = \mathcal{L} \cdot \frac{\beta^*_x \beta^*_y}{\sqrt{\beta^{*2}_x + s^{*2}_x}\sqrt{\beta^{*2}_y + s^{*2}_y}} . \quad (20)$$

By inserting the data from Table V in Equation 20, one gets another measure of the improvement brought by the implementation of the linear optics correction:

$$\begin{aligned} G^{\mathrm{IR6}}_{measured} = 0.980 \Rightarrow G^{\mathrm{IR6}}_{corrected} = 0.997 \ ; \\ G^{\mathrm{IR8}}_{measured} = 0.919 \Rightarrow G^{\mathrm{IR8}}_{corrected} = 0.949 \ . \end{aligned} \quad (21)$$

In addition to those corrections, an $s^*_{x,y}$ knob has been developed for RHIC to provide additional control on the delivered luminosity [21], more specifically with the goal of achieving luminosity leveling both for RHIC and its upgrade to an electron-ion collider, eRHIC [22].

B. First experiments with the dynamic β^* squeeze

The first attempt at squeezing $\beta^*_{x,y}$ below the design value of 0.70 m was performed right after the implementation of the linear optics correction described in the previous section. Since all these activities are taking place during specific time periods dedicated to machine experiments, the transverse beam emittances $\epsilon_{x,y}$ cannot be

TABLE V. Amplitude of the $\beta_{x,y}$ functions at the interaction point (IP) of the STAR and PHENIX experiments for the 2014 Blue lattice, before and after linear optics corrections. These values are calculated from fitting $\beta_{x,y}$ between the nearby Q_1 triplet quadrupole magnets located around each IP. The lowest values $\beta^*_{x,y}$ over that range, as well as their distance $s^*_{x,y}$ to the IP, are also given. In the 2014 lattice design, $\beta_{x,y}$(IP)= $\beta^*_{x,y} = 0.70$ m.

Parameter	**IR6 (STAR)** measured / corrected	**IR8 (PHENIX)** measured / corrected
β_x(IP) [m]	0.844 / 0.741	0.772 / 0.734
β_y(IP) [m]	0.671 / 0.709	0.796 / 0.771
β^*_x [m]	0.844 / 0.738	0.677 / 0.706
β^*_y [m]	0.645 / 0.707	0.767 / 0.722
s^*_x [m]	0.017 / -0.049	0.253 / 0.141
s^*_y [m]	-0.129 / 0.034	-0.149 / 0.188

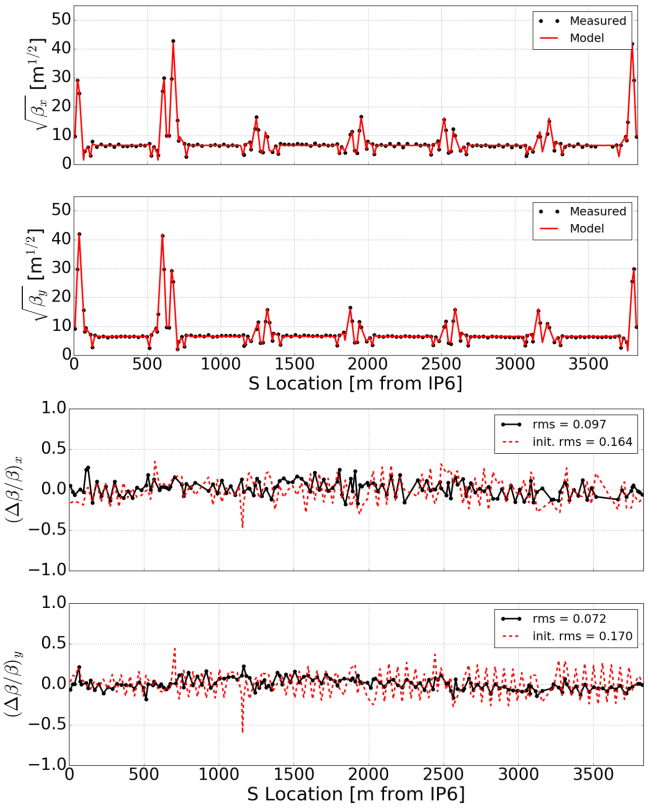

FIG. 13. Top: Measured horizontal (top) and vertical (bottom) $\sqrt{\beta}$ functions for the 2014 Blue Au-Au 100 GeV lattice (Fill #18127) compared to their design values from the RHIC Online Model after implementation of the calculated linear optics correction. - Bottom: corresponding horizontal (top) and vertical (bottom) β-beat amplitude, compared to the initial measurement. The *rms* values of the deviations are given for each plane. There is a significant improvement compared to the uncorrected linear optics. All reported values are derived from the analysis of turn-by-turn closed orbit oscillations acquired at every BPM locations around the ring.

reduced by the RHIC Stochastic Cooling system since it would required about 2 additional hours to do so, according to the data shown in Figure 1. It was therefore decided to adopt a cautious, staged approach in order to reach the target of $\beta^*_{x,y} = 0.5$ m. Being in the commissioning phase and with limited time available, it is important to minimize beam losses to avoid pulling the permit link of the RHIC machine protection system which would drop a ramp attempt, therefore:

- only 6 bunches (out of a possible 111) with regular intensity are brought to 100 GeV, with the added benefit of limiting the risks of losses related to collective effects;
- to allow controlling chromatic effects (both linear and non-linear), lattices are squeezed in 10 cm steps: $\beta^*_{x,y} = 0.70$ m $\rightarrow 0.60$ m $\rightarrow 0.50$ m;
- only one lattice at a time is squeezed.

During this commissioning process, the beam lifetime had to be adjusted after each $\beta^*_{x,y}$ squeeze step, due to off-momentum losses: to ensure solid beam dynamics at injection, all RHIC dipole magnets in the arcs had to be displaced by an offset dx of 50 mil inches (1.27 mm) in the horizontal plane [23], in turns generating a betatron tune feed-down effect from the non-linear sextupole field errors $K_2^{\rm err}$ (inherent to construction) present in those dipoles. This feed-down effect can be modeled as an additional quadrupole gradient $K_1^{\rm err} = K_2^{\rm err} \cdot dx$, contributing to the linear chromaticity by a term $Q'^{\rm err}_{x,y}$ that has to be added to the definition from Equation 9 given in Section II C:

$$Q'^{\rm err}_{x,y} = \frac{1}{4\pi} \oint \mp \beta_{x,y}(s) K_1^{\rm err}(s) ds \ . \qquad (22)$$

In the context of rematching linear optics and chromaticities for the squeezed lattices, the $\beta_{x,y}(s)$ functions in the ATS region (as defined in section II B) will be affected by the required β-beat wave, altering $Q'^{\rm err}_{x,y}$. It is therefore highly relevant to include Equation 22 in the MAD-X model used for lattice design[3].

[3] the RHIC online model, made of the RampManager and OptiCalc servers, does include the feed-down contribution to chromaticity; this was one of the main sources of disagreement between offline and online modeling.

Prior to 2014, reports from the STAR experiments indicated that parts of their sensitive material (hardware electronics and silicon plates) were severely damaged during previous high energy runs when abort kicker modules would pre-fire, which is not acceptable. A preventive solution was developed in order to drive the bunches affected by the pre-fire event into the cold aperture, using closed orbit bumps in the arc immediately downstream of the beam abort insertion (IR10, see Figure 3) following the beam direction [24], as shown in Figure 14.

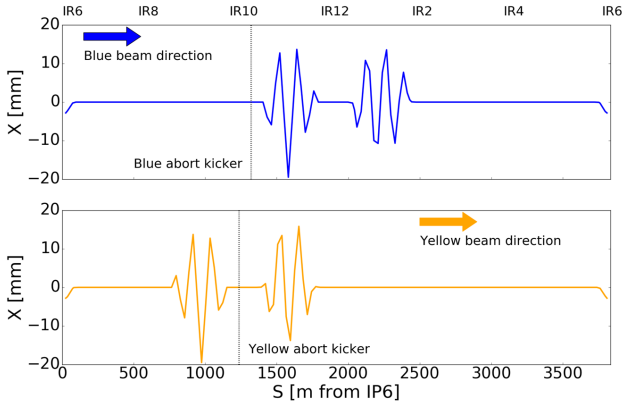

FIG. 14. Closed orbit bump for the Blue (top) and Yellow (bottom) beam in RHIC for abort kicker prefire protection.

These bumps bring additional offsets $dx_{\rm orb}(s)$ inside of the arc dipoles, which in turn generates another chromaticity term $Q'^{\,\rm orbit}_{x,y}$ similar to the one described in Equation 22 that must be accounted for when trying to minimize the chromaticity changes during the dynamic β^* squeeze:

$$Q'^{\,\rm orbit}_{x,y} = \frac{1}{4\pi}\oint \mp\beta_{x,y}(s)K_2^{\rm err}(s)dx_{\rm orb}(s)ds\ . \qquad (23)$$

Once the sextupole strengths were adjusted to take care of off-momentum losses and improve the beam lifetime to a loss rate better than 10% per hour (a self-imposed criteria for this experiment), it was possible to measure the new, squeezed linear optics. Figure 15 presents the β-beating data for the β^*(IP6,IP8) = 0.60 m and β^*(IP6,IP8) = 0.50 m settings, derived from data taken on two separate fills. Table VI shows the interpolated $\beta_{x,y}$ functions at the IP as well as their minima $\beta^*_{x,y}$ for the STAR (IR6) and PHENIX (IR8) experiments; Table VII lists all *rms* values for comparison with the initial, uncorrected lattice. Although it is clear that the lattice gets worse when reaching β^*(IP6,IP8) = 0.50 m, the *rms* β-beat is on par with that of the uncorrected β^*(IP6,IP8) = 0.70 m lattice used for RHIC physics. As mentioned earlier, data is only provided for the Blue lattice of RHIC for practical purposes; however results were very similar for the Yellow lattice, which also achieved β^*(IP6,IP8) = 0.50 m. The dynamic squeeze ramp is therefore ready for implementation into regular beam operations.

TABLE VI. Interpolated $\beta_{x,y}$ functions (from measurements) at and around the IP marker for the STAR (IR6) and PHENIX (IR8) experiments.

Target β^*		**IR6 (STAR)**	**IR8 (PHENIX)**
[m]		$\beta^*/\beta\,(\mathrm{IP})/s^*$ [m]	$\beta^*/\beta\,(\mathrm{IP})/s^*$ [m]
0.600	(H)	0.568/0.573/-0.051	0.631/0.632/-0.026
	(V)	0.580/0.581/-0.024	0.611/0.621/-0.081
0.500	(H)	0.461/0.516/-0.159	0.466/0.478/-0.075
	(V)	0.480/0.512/0.123	0.511/0.511/-0.019

TABLE VII. Measured changes in *rms* $\beta_{x,y}$-beating for the Blue lattice after linear optics correction and each step of the dynamic β^* squeeze process.

β^***(IP6,IP8)**	**Horizontal** ***rms***	**Vertical** ***rms***
0.70 m (physics)	0.164	0.170
0.70 m (corr.)	0.097	0.072
0.60 m	0.065	0.052
0.50 m	0.169	0.087

C. Changes to machine protection settings

Since the goal of the dynamic squeeze is to increase the delivered luminosity to the experiments, keeping the inherent background in check for the squeezed settings is of utmost importance. Another critical parameter is the beam loss rate during the ramp to the squeezed settings, since losing too much beam would counteract the benefits of lower $\beta^*_{x.y}$ values.

To address both of these issues, two RHIC systems that were not used during dedicated beam experiment periods need to be considered. One is the collimation system, located around PHENIX (IR8) for background control: it is made of a group of horizontal and vertical blocks (also called *jaws*) of copper to limit the size of the transverse halo, typically to 5-8 $\sigma_{x,y}$ for RHIC. The other system is the Stochastic Cooling: since the β-beat wave generated to achieve the dynamic squeeze extends into sectors of the Blue and Yellow lattices where its equipment is located, the available mechanical aperture has to be checked.

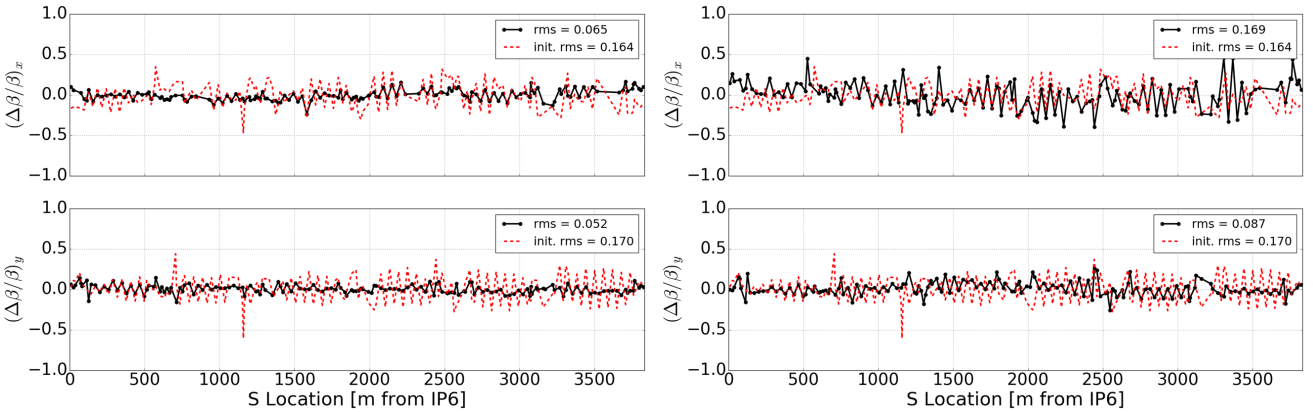

FIG. 15. Left: Horizontal (top) and vertical (bottom) β-beat amplitude for the $\beta^* = 0.60$ m optics. The *rms* values of the deviations are given for each plane. - Right: Horizontal (top) and vertical (bottom) β-beat amplitude for the $\beta^* = 0.50$ m optics. The *rms* values of the deviations are given for each plane. All reported values are derived from the analysis of turn-by-turn closed orbit oscillations acquired at every BPM locations around the ring.

1. *Collimators settings*

The positions of the collimator jaws are set up to intercept particles in the beam halo, maintaining the beam-induced background to within tolerable levels for the STAR and PHENIX detectors and providing protection to the superconducting components of the accelerator. It is necessary to ensure that there is no increase in beam loss during the β^* squeeze due to increasing halo size: if the halo gets too large too fast, the sudden, however transient spike in the beam loss rate could trigger a permit pull aborting the beam. Table VIII shows the $\beta_{x,y}$ functions at the locations of the primary collimators for the $\beta^* = 0.70$ m and $\beta^* = 0.50$ m lattices. As mentioned in Section II B, the beam envelope gets significantly larger at the triplet quadrupoles in IR6 and IR8 in a lattice with the ATS.

TABLE VIII. $\beta_{x,y}$ functions at the locations of the (B)lue and (Y)ellow primary collimators for the baseline $\beta^* = 0.70$ m lattice and the squeezed $\beta^* = 0.50$ m lattice.

β^***(IP6,IP8)**	β_x**(coll.)**	β_y**(coll.)**
0.70 m	(B) 1417.23 m	(B) 465.40 m
	(Y) 1429.43 m	(Y) 480.90 m
0.50 m	(B) 2063.09 m	(B) 661.88 m
	(Y) 2196.34 m	(Y) 695.64 m

The calculated increases in $\beta_{x,y}$ functions at the collimators range from 42% (Blue vertical) up to 54% (Yellow horizontal). These squeezed lattice optics have to be put in context though: they are implemented late in a physics store, around the time that the transverse beam emittances reach equilibrium from the effect of Stochastic Cooling. From the data shown in Figure 1, one can take $\epsilon_{\rm SC} = 0.65$ μm at the equilibrium: the 5 $\sigma_{x,y}$ envelope therefore increases by at least 1.6 mm (Blue vertical) and as much as 3.5 mm (Yellow horizontal) for the squeezed lattice. These numbers actually compare to a 1 $\sigma_{x,y}$ increase if one considers the baseline lattice optics, well within the tolerance of the RHIC collimation system. The tightest mechanical aperture in the machine remains at the collimator locations, and the jaws positions would only have to be readjusted if the background levels spike.

2. *Stochastic Cooling kickers*

Spurious events can still drive the beam halo into the mechanical aperture of the elements with the tightest transverse openings. At the same time, in order for the SC system to operate, the kickers must be able to close their split cavities, leaving an opening as tight as 2 cm full width. This creates additional aperture limitations around the RHIC rings.

Figure 3 shows that there is some SC equipment located in IR4, an insertion that is used for setting up the dynamic β^* squeeze: the Blue longitudinal kicker and transverse pickups, and the Yellow transverse kickers. Contrary to the collimator jaws which are built to intercept particles with large deviations in all three planes of motion, the mechanical design and construction material of the SC kickers and pickups are not made to withstand large amounts of energy deposition due to local beam losses. Thus even if the on-momentum beam size would fit within the available 2 cm aperture, one has to account for the momentum offset $\Delta p/p_0$ and the dispersion function D_x, making the transverse beam sizes:

$$\sigma_{x,y}^{\rm mom}(s) = \sqrt{\beta_{x,y}(s)\cdot\epsilon_{\rm SC} + \left(D_{x,y}(s)\cdot\frac{\Delta p}{p_0}\right)^2}\ . \quad (24)$$

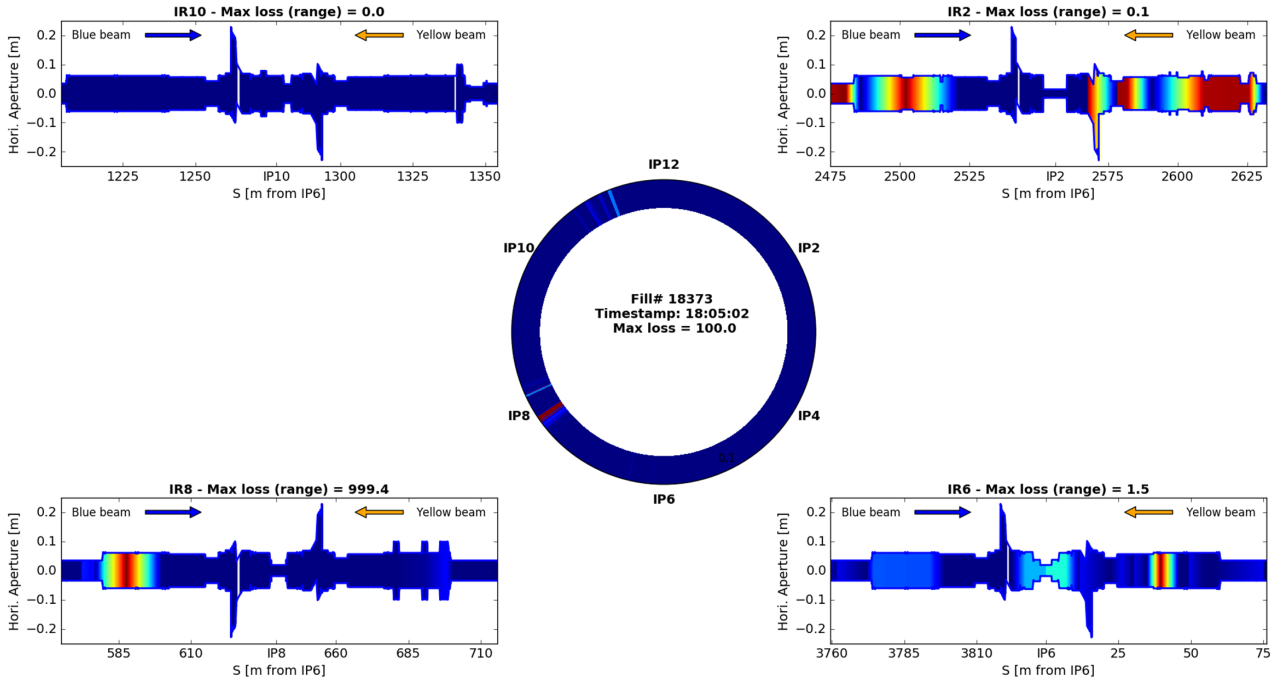

FIG. 16. Longitudinal beam loss map in RHIC (center) and in each IR (corners) during an end-of-store dynamic β^* squeeze attempt. The signal from BLM's is displayed as a color map filling the horizontal mechanical aperture of the Blue ring, for reference purposes. Loss signals within each IR are scaled to the peak value in that area.

TABLE IX. $\beta_{x,y}$ and D_x functions at the locations of the Blue (top) and Yellow (bottom) Stochastic Cooling equipment in the ATS region of the squeezed $\beta^* = 0.50$ m lattice (IR4-IR10). The momentum offset used to determine the beam size via Equation 24 is $\Delta p/p_0$ =1.8e-3.

Name	β_x [m]	β_y [m]	D_x [m]	Max. beam size 5 $\sigma_{x,y}^{\rm mom}$ [cm]
bo3-cpuv3	18.56	42.31	0.162	0.25
bo3-cpuh3	57.17	226.22	-0.076	0.59
bi4-kscl3.1	37.38	10.37	-0.034	0.24
bi4-kscl3.2	34.20	12.16	-0.043	0.23
bi4-kscl3.3	31.24	14.33	-0.053	0.22
yi3-kscv3	13.08	36.33	0.005	0.23
yi3-ksch3.2	13.78	26.97	0.045	0.20
yi3-ksch3.1	14.49	23.46	0.062	0.19

Table IX lists the optic functions for the SC equipment located within the ATS region of the $\beta^* = 0.50$ m Blue and Yellow lattices, along with the largest value of the 5 $\sigma_{x,y}^{\rm mom}$ beam size (between the horizontal and vertical plane). The momentum offset typically considered for dynamic aperture simulations in RHIC is taken as $\Delta p/p_0$ =1.8e-3, and is also used here for the calculation of $\sigma_{x,y}^{\rm mom}$. For both the Blue and Yellow ATS lattices, the estimated maximum beam size remains well within the available aperture of the SC equipment.

IV. OPERATIONAL IMPLEMENTATION & MEASURED LUMINOSITY CHANGES

Once all commissioning experiments described in Section III are successfully completed, the next step is to implement the dynamic β^* squeeze as part of the regular 100 GeV Au-Au operations. When dealing with a filled machine (111 bunches in each beam), the safest approach is to ramp to the squeezed lattices settings as part of an end-of-store activity, i.e. just before beams are aborted due to low intensity. At that time the transverse beam emittances have already reached their low equilibrium ($\epsilon_{\rm SC} = 0.65$ mm) and the SC cavities are still closed, the expectation being that the mechanical apertures of these cavities are wide enough to avoid local beam losses. As a precaution, it was recommended to pause the SC system and open the assemblies on the first few attempts at engaging the dynamic squeeze.

Tune and chromaticity corrections are needed to make sure to minimize beam losses. Figure 16 shows the longitudinal loss pattern around RHIC during one of the last end-of-store attempts: the only significant loss rates are reported in the IR8 insertion where the collimation

system for the Yellow beam is located. This diagnostic allows proceeding safely with the operational implementation.

One last parameter to determine is when to activate the dynamic β^* squeeze. In 2014, beams were stored for collisions at $\sqrt{s_{NN}} = 200$ GeV for ten hours; with substantial improvements over the years in both the injected bunch intensity and the beam lifetime during the ramp in energy, each physics fill would start with high collision rates at both STAR and PHENIX experiments. Early diagnostics showed that there were triggering issues in the data acquisition system of the Heavy Flavor Tracker (HFT) part of the STAR detector: the target rate for the Zero Degree Calorimeter (ZDC) was therefore dropped to 50 kHz two and a half hours into each store to allow both high and low luminosity goals to be reached. In that context, the dynamic squeeze can only be implemented if it does not increase the STAR ZDC rate over 50 kHz, but also not too late into each store that the added contribution to the integrated luminosity can remain substantial. The decision was then made to have the dynamic β^* squeeze part of the regular beam operations seven hours into each physics store for the last two weeks of the RHIC Run14 100 GeV Au-Au program.

Figure 17 presents the collision rates in the STAR and PHENIX interaction regions over the course of a 2014 physics store for Au-Au collisions at $\sqrt{s_{NN}} = 200$ GeV. One can notice luminosity leveling effort of the STAR rates, achieved by introducing a vertical separation bump between the circulating beams. This bump is controlled by the same process that maintains head-on collisions over the duration of a physics store, compensating for position drifts via the feedback systems - except the beams are forced apart in the case of rates leveling. A marker is added to indicate when the β^* squeeze ramp is activated.

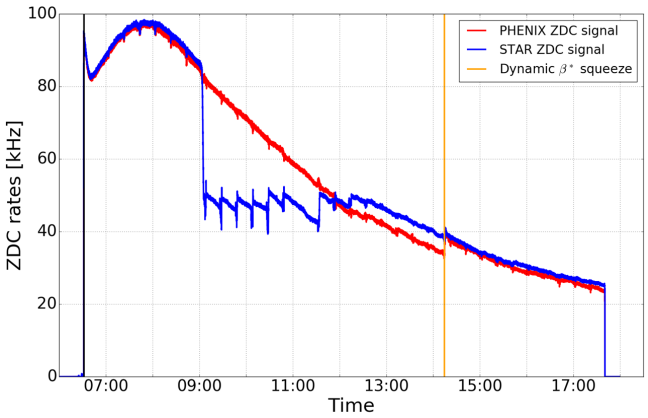

FIG. 17. Profile of the ZDC collision rates for the STAR and PHENIX experiments over the course a single store for Au-Au collisions at $\sqrt{s_{NN}} = 200$ GeV in 2014. The STAR collision rate is dropped to 50 kHz to allow the experiment to reach both its high and low luminosity goals. A marker (yellow line) points to when the dynamic β^* squeeze is activated.

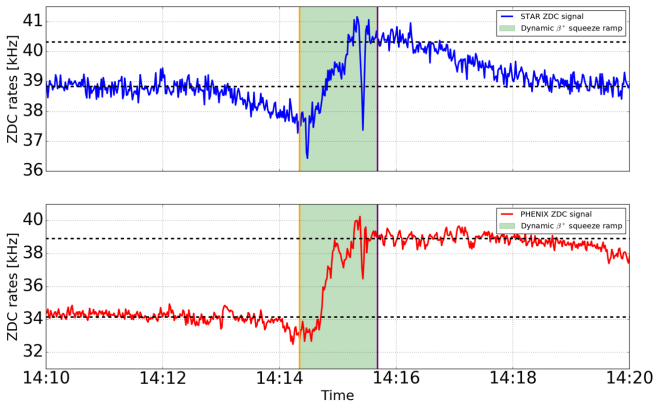

FIG. 18. Zoom of Figure 17 around the time at which the dynamic β^* squeeze ramp is engaged. Dashed lines are added to highlight the "before" and "after" ZDC rates used to calculate the relative luminosity increase for each experiment.

Looking closer at the ZDC rates before and after the squeeze ramp, as displayed in Figure 18, one can calculate the relative change in luminosity, and compare it to what can be predicted by using data from linear optics measurements into Equation 14. Because of the difference in beam sizes between the Blue and Yellow beams at each interaction point, it becomes relevant to work under a "round beams" assumption by determining a β^* equivalent based on the overlap between the two colliding beams. Figure 19 shows the 3 $\sigma_{x,y}$ beam size for both STAR and PHENIX based on the *rms* values of $\beta_{x,y}$ at each location derived by a series of measurements, performed during the commissioning steps described in Section III. The final beam sizes after the dynamic squeeze, determined with a similar process, are included for comparison purposes.

In the case of STAR, one can clearly see that the overlapping cross-section between the Blue and Yellow beam is smaller than either beam size: for the purpose of theoretical predictions, this area will be taken as a circle with a β^* equivalent of:

$$\beta^*\,(\text{STAR}) = \sqrt{\beta_x\,(\text{Yellow}) * \beta_y\,(\text{Blue})}\,. \qquad (25)$$

As for PHENIX, since the Yellow beam seem consistently larger than the Blue beam at this particular IP, only $\beta_{x,y}\,(\text{Blue})$ will be considered in our calculations.

$$\beta^*\,(\text{PHENIX}) = \sqrt{\beta_x\,(\text{Blue}) * \beta_y\,(\text{Blue})}\,. \qquad (26)$$

Based on Equation 14, the ratio pre/post-squeeze $\mathcal{R}$ of the luminosity at a given IP reads:

$$\mathcal{R} = \frac{\mathcal{L}_{post}}{\mathcal{L}_{pre}} = \frac{H_{post}}{H_{pre}} . \frac{\beta^*_{pre}}{\beta^*_{post}}\,, \qquad (27)$$

with β^*_{pre} and β^*_{post} the pre- and post-squeeze $\beta^*_{x,y}$ equivalents under the round beam approximation.

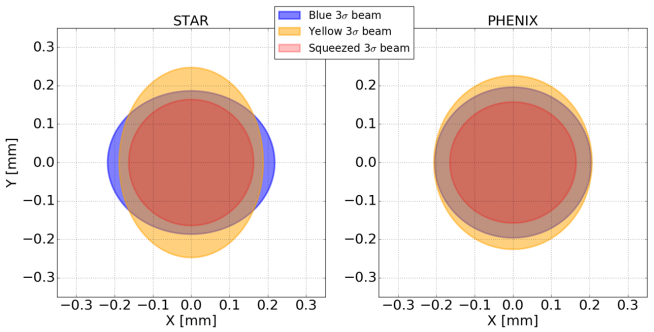

FIG. 19. Pre- and post-squeeze 3 $\sigma_{x,y}$ *rms* beam sizes at the STAR and PHENIX IPs. Only the overlapping areas between the Blue and Yellow beams will be considered for the theoretical predictions of the luminosity increase.

TABLE X. Theoretical prediction of the luminosity increase due to dynamic β^* squeeze during RHIC Run14 for the STAR and PHENIX experiments. Linear optics functions are derived from measurements done during the experimental commissioning of the squeeze ramp.

Experiment	**STAR**	**PHENIX**
β^*_{pre} *rms* [m]	0.679	0.796
H_{pre}	0.434	0.483
β^*_{post} *rms* [m]	0.525	0.509
H_{post}	0.361	0.373
$\mathcal{R}$ [%]	**+7.65% (±2.50%)**	**+14.51% (±4.70%)**

Table X summarizes the estimated values of all variables from Equations 25, 26 and 27, and gives the estimated, theoretical value of $\mathcal{R}$ for STAR and PHENIX for the RHIC Run14 dynamic β^* squeeze configuration. The Hourglass coefficient H is calculated assuming head-on collisions with an *rms* bunch length of 6.49 ns and transverse *rms* emittances $\epsilon_{x,y} = 0.616$ μm - these values are based on typical Run14 data around the time the β^* squeeze ramp was used during a given physics store. As a result, one gets predicted increases of $\mathcal{R}$(STAR) = +7.65% and $\mathcal{R}$(PHENIX) = +14.51% respectively. The discrepancy between the two experiments is illustrated by the change in overlapping beam sizes shown in Figure 19 where the PHENIX effective cross-section is initially larger than the one at STAR.

After being declared fully operational, the dynamic β^* squeeze ramp was used for nine full physics stores. One can determine the pre- and post-squeeze ZDC rates by taking the *rms* of these rates over a given sample of time, in this case 60 seconds. Such sample must be grabbed under physics conditions, i.e. with the feedback systems still running before they are turned off as part of the setup for the squeeze ramp. Noticing the change of slope in the STAR rates in Figure 18, the pre-squeeze rates sample will be taken as the interval of time from 150 to 90 seconds away from the start of the squeeze ramp.

Looking at these nine physics store, Table XI compiles the pre- and post-squeeze ZDC rates and the corresponding ratios. One can determine the corresponding error bars based on the sampling method described above. Having done so, all data points can be plotted and compared to the theoretical predictions from Table X, which is done via Figure 20. The predicted luminosity increase for each experiment is very close to the calculated *rms* over the nine physics store analyzed, with differences of less than 1%. For completeness, a colored area around both $\mathcal{R}$(STAR) and $\mathcal{R}$(PHENIX) is included to represent the error bars due to the measured linear optics, both systematics and store-to-store variations. These areas highlight the fact that, even when accounting for all measurement uncertainties (optics and collision rates), the achieved luminosity increase during RHIC Run14 was well within the expected values - to the exception of the outlier Fill 18417.

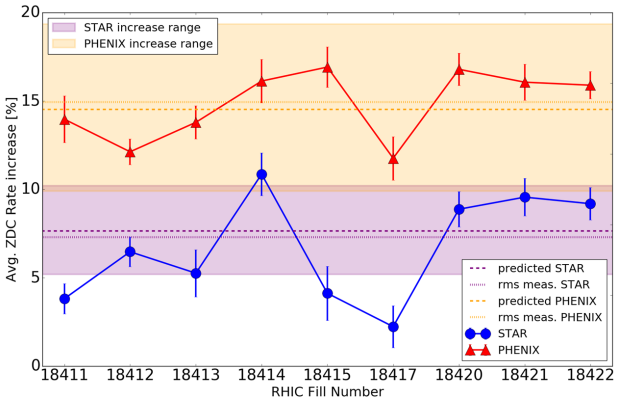

FIG. 20. Comparison between the predicted luminosity increases $\mathcal{R}$(STAR,PHENIX) and the measured changes in collision rates for the nine physics store for which the dynamic β^* squeeze was used. The colored areas represent the uncertainty in $\mathcal{R}$ due to the variations in linear optics measurements: the calculated predictions still manage to include every measured ZDC data points except Fill 18417, a clear outlier for both experiments.

V. CONCLUSION

Taking advantage from the performance of the RHIC Stochastic Cooling system, a dynamic β^* squeeze mechanism was developed based on the principle of the Achromatic Telescopic Squeeze designed for the LHC at CERN.

TABLE XI. Relative increase in ZDC rates for the STAR and PHENIX experiments due to the dynamic β^* squeeze. These *rms* values are based on a sampling of the collision rates over 60 seconds before and after the squeeze.

Fill No.	**18411**	**18412**	**18413**	**18414**	**18415**	**18417**	**18420**	**18421**	**18422**
STAR									
Before [kHz]	38.83	45.20	48.24	37.91	50.44	42.67	43.38	43.78	40.79
After [kHz]	40.31	48.12	50.77	42.02	52.51	43.62	47.24	47.97	44.54
Ratio [%]	+3.81	+6.47	+5.26	+10.86	+4.12	+2.23	+8.87	+9.56	+9.19
***rms* over all Fills**	**+7.29%**	**(predicted: +7.65%±2.50%)**							
PHENIX									
Before [kHz]	34.14	45.40	49.31	39.80	50.17	41.24	42.57	43.90	40.42
After [kHz]	38.91	50.90	56.11	46.22	58.66	46.09	49.72	50.96	46.84
Ratio [%]	+13.97	+12.12	+13.79	+16.13	+16.92	+11.76	+16.79	+16.06	+15.89
***rms* over all Fills**	**+14.94%**	**(predicted: +14.51%±4.70%)**							

The goal is to increase the delivered integrated luminosity to the STAR and PHENIX experiment by lowering the linear $\beta^*_{x,y}$ at the interaction point from 0.70 m to 0.50 m (design values). Working with the existing hardware and power supply wiring scheme, numerical simulations and modeling tools are used to calculate the required quadrupole strength changes, along with the required baseline linear optics corrections as well as a minimization of the non-linear chromatic imperfections. After going through experimental commissioning sessions with dedicated beam time, it was determined that the squeezed optics could be implemented operationally without significantly increased risks of damages to the most sensitive equipment of the collider. Once declared fully operational, the resulting luminosity increases as given by the relative changes in collision rates for each experiment was compared to the theoretical predictions made by taking into account the pre- and post-squeeze Hourglass factors: the agreement is better than 1% on the *rms* values, and even store-to-store variations fall within the estimated error bars derived from multiple linear optics measurements. These results demonstrate the successful design and implementation of the dynamic β^* squeeze mechanism specific to the RHIC high energy lattices. This mechanism is now being relied upon for the design of the beam parameters that will be utilized to deliver high luminosity collisions to eRHIC experiments.

[1] CERN Accelerator School: Intermediate Course on Accelerator Physics, Zeuthen, Germany, 15-26 September 2003, p. 361-378 (2006).
[2] M. Blaskiewicz, J. M. Brennan, and F. Severino, Phys. Rev. Lett. **100**, 174802 (2008).
[3] M. Blaskiewicz, J. M. Brennan, and K. Mernick, Phys. Rev. Lett. **105**, 094801 (2010).
[4] M. Blaskiewicz, J.M. Brennan, and K. Mernick, Proc. of COOL2013, Murren, Switzerland, 6 (2013).
[5] RHIC Run Overview, http://www.agsrhichome.bnl.gov/RHIC/Runs/
[6] A. Drees et al., Proc. of PAC07, Albuquerque, NM, USA, 722 (2007).
[7] G. Robert-Demolaize at al., Proc. of IPAC12, New Orleans, LA, USA, 1314 (2012).
[8] *RHIC Design Manual*, p. 269 (2006).
[9] W. Fischer et al., Phys. Rev. Lett. 115, 264801 (2015).
[10] X. Gu et al., Phys. Rev. Accel. Beams **20**, 023501 (2017).
[11] S. Fartoukh, Phys. Rev. Accel. Beams **16**, 111002 (2013).
[12] S. Fartoukh et al., J. Phys.: Conf. Ser. **874**, 012010 (2017).
[13] Y. Luo et al., Proc. of IPAC'13, Shanghai, China, 1538 (2013).
[14] K. Mernick, M. Blaskiewicz, J.M. Brennan, Proc. of NA-PAC13, Pasadena, CA, USA, 41 (2013).
[15] MAD-X documentation, http://madx.web.cern.ch/madx/.
[16] Y. Luo, X. Gu, W. Fischer, D. Trbojevic, RHIC C-AD Internal Note, C-A/AP/418 (2011).
[17] R. Tomás et al., Phys. Rev. Accel. Beams **20**, 054801 (2017)
[18] G. Robert-Demolaize, M. Bai and X. Shen, Proc. of NA-PAC13, Pasadena, CA, USA, 472 (2013).
[19] R.E. Meller et al., SSC-N-360 (1987).
[20] W. H. Press *et. al.*, *Numerical Recipes in C* (2nd ed.), *Ch 15.5 Modeling of Data / Nonlinear Models*, Cambridge University Press (1992).
[21] Y. Hao et al., Proc. of IPAC'15, Richmond, VA, USA, 2357 (2015).
[22] V. Ptitsyn et al., Proc. of EPAC'04, Lucerne, Switzerland, 923 (2004).
[23] S. Peggs et al., RHIC C-AD Internal Note, C-A/AP/62 (1995).
[24] G. Robert-Demolaize et al., Proc. of IPAC'14, Dresden, Germany, 1090 (2014).